Delft University of Technology

Influences of Nanostructures of Sn and Ir for the Oxygen Evolution Reaction in Polymer Electrolyte Membrane Water Electrolysis

Bunea, Sorin; Li, Min; Demiröz, Ezgi; Zeng, Peng; Willinger, Marc Georg; Urakawa, Atsushi

Important note
To cite this publication, please use the final published version (if applicable).
Please check the document version above.

Article

Influences of Nanostructures of Sn and Ir for the Oxygen Evolution Reaction in Polymer Electrolyte Membrane Water Electrolysis

Sorin Bunea, Min Li, Ezgi Demiröz, Peng Zeng, Marc Georg Willinger, and Atsushi Urakawa*

Cite This: *Energy Fuels* 2024, 38, 637–646

Read Online

ACCESS | Metrics & More | Article Recommendations | Supporting Information

ABSTRACT: The influence of nanostructures and interaction of Sn and Ir in oxygen evolution catalysts in a polymer electrolyte membrane electrolyzer were investigated. For this aim, two synthesis methods, namely, the one-step solution combustion method and the precipitation–deposition method with sodium borohydride reduction, were evaluated to prepare distinct nanostructures. Sn addition to Ir-based oxygen evolution reaction catalysts has been reported to yield materials with higher activity; however, in our case, this was observed only for Sn/Ir catalysts prepared by the precipitation–deposition method. The nanolayer of Sn/SnO$_2$ deposited over metallic Ir particles was identified to enhance the interfacial contacts, resulting in synergistic interactions. By deconvolution of the polarization curves into constituting contributions, the performance improvement was attributed to the higher exchange current density of the Sn/Ir powder as a consequence of a higher number of surface reaction sites created by the Sn–Ir interactions.
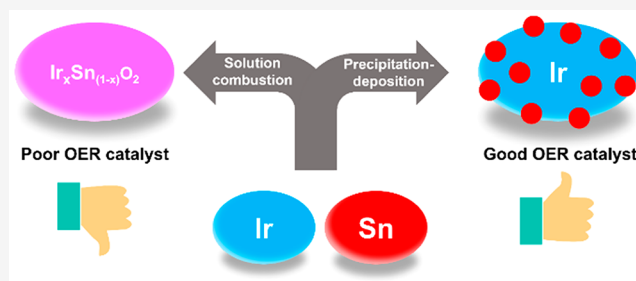
1. INTRODUCTION

Electricity generation from renewable wind and solar energy has steadily increased in the past decade.[1] Nevertheless, greater efforts are required for renewable energy sources to become the primary energy sources for humanity. One of the major challenges toward achieving this ambitious goal is the intermittent nature of solar and wind energy, often asynchronous with electricity demand. The adoption of a "hydrogen economy" could represent a solution to mitigate the aforementioned challenges.[2] In such an approach, electrical energy can be converted into chemical energy via water electrolysis, yielding hydrogen, which can be stored and used on demand for electricity production via fuel cells or simply clean combustion, producing only water.

Polymer electrolyte membrane (PEM) electrolysis possesses a series of advantages over alkaline electrolysis, which makes it particularly attractive for commercial implementation. Some representative advantages are (i) high faradaic efficiency as a result of a low gas crossover rate between cathode and anode compartments, (ii) ability to operate at high current densities, (iii) low ohmic resistance, (iv) robust and compact cell design, and (v) possibility of yielding hydrogen at elevated pressures.[3] Although a decrease in the PEM electrolyzer price was witnessed over the past 30 years, a few drawbacks still limit the wide applicability of PEM technology.[4] One of the most important limitations is the need for costly and scarce noble metal electrocatalysts, such as platinum, ruthenium, and/or iridium. Efforts in decreasing the loading of these metals are ongoing in the scientific community.[5−10] Particularly, replacing state-of-the-art iridium as an anode electrocatalyst in PEM electrolyzers has been proven difficult, because the requirements for alternative catalyst candidates are not limited to high activity toward the oxygen evolution reaction (OER) (eq 1) but also demand long-term stability in the acidic anodic environment of the PEM electrolyzer. The main efforts in the scientific community regarding the anode side of PEM electrolyzers are focused on improving iridium dispersion using various support materials, engineering the catalyst layer morphology to increase the surface area, porosity, and contact between components, employing core–shell structures with a reduced iridium content, decreasing the catalyst particle size, and recycling iridium.[11−23]

$$2H_2O \rightarrow O_2 + 4H^+ + 4e^- \tag{1}$$
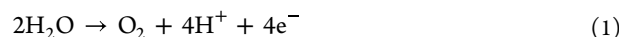
Of various support materials proposed in the literature, antimony-doped tin oxide (ATO) has been investigated extensively, because it provides good electric conductivity and stability in anodic conditions.[24−26] Furthermore, recent publications suggest that tin(IV) oxide does not merely play the role of a support, as reported earlier, but rather takes part in electrocatalysis.[27−30]
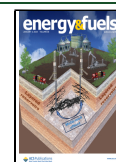
In this work, we have examined potential synergies of Ir and Sn for the OER in a PEM electrolyzer. Two different material synthesis strategies were studied. The first strategy is solution combustion synthesis (SCS), which is a facile one-step synthesis method to produce nanodispersed materials, as demonstrated by high Ir/IrO_2 dispersion in an Al_2O_3 matrix.[31] The second strategy is the precipitation−deposition method. In contrast to most literature studies based on the deposition of active iridium metal over a tin oxide/antimony-doped tin oxide support, we took an opposite approach by depositing tin over iridium nanoparticles.[12,13,24,25] In this way, the active Ir surface is expected to be covered with SnO_2 and should point out the existence of the synergy. We show how Ir/IrO_2 interacts with SnO_2 on the nanoscale matter and the synergy of Ir and Sn interactions for OER.

2. EXPERIMENTAL SECTION

2.1. Catalyst Synthesis. $Ir_xSn_{1-x}O_2$ powders were synthesized via a solution combustion method. $IrCl_3 \cdot xH_2O$ (99.9%, Precious Metals Online, Ltd.) and $SnCl_4 \cdot 5H_2O$ (98%, Sigma-Aldrich) were used as metal precursor salts. Glycine (99%, Alfa Aesar) was used as fuel, and ammonium nitrate (Sigma-Aldrich) was used as the oxidizing agent. A stoichiometric ratio of components, according to the φ parameter (φ = 1), described elsewhere, was used.[32] The components were mixed together and dissolved in 10 mL of water in a porcelain crucible. The mixture was stirred on a heating plate at 90 °C until the water evaporated and a gel formed. After the gel formation, the crucible was transferred to a preheated furnace at 90 °C, and the temperature was ramped up to 500 °C, at a rate of 10 °C min^{-1}, and held at this temperature for 3 h for the calcination of the powders and removal of carbon compounds, which might have remained after the combustion. The obtained powders were used as the OER catalysts without any further treatment steps.

Sn/Ir powders were synthesized via a precipitation−deposition method. In the first step, iridium black powder was prepared from $IrCl_3 \cdot xH_2O$, according to the procedure described in the literature.[33] The powder was dried at 120 °C overnight. Subsequently, the iridium black powder was suspended in 100 mL of ultrapure water in a flask. $SnCl_4 \cdot 5H_2O$ was added, and the flask was stirred until complete dissolution of $SnCl_4 \cdot 5H_2O$. The flask was transferred to an ultrasonic bath, and 6-fold excess $NaBH_4$ (98%+, Acros Organics) powder was slowly added. When gas evolution was no longer observed, the powder was washed with 1 L of ultrapure water and dried at 120 °C overnight.

2.2. Catalyst Characterization. N_2 physisorption experiments were performed using a Micromeritics Tristar 3020 setup after an overnight degassing step at 150 °C. X-ray diffractograms of the powders were recorded with a Bruker D8 Discover powder diffractometer with a Cu Kα radiation source.

Transmission electron microscopy (TEM) was recorded with a JEOL JEM-1011 microscope. High-resolution transmission electron microscopy (HRTEM) images were acquired using a JEOL Grand ARM operated in scanning/transmission electron microscopy (S/TEM) mode at 300 kV and a Thermo Fisher Scientific Titan Themis operated in STEM mode at 300 kV. Energy-dispersive X-ray spectroscopy (EDS) mapping was performed at both instruments in STEM mode.

2.3. Membrane Electrode Assembly (MEA) Preparation and Cell Assembly. Nafion 115 membranes (Ion Power) were used for all experiments. The membranes were pretreated in 3 wt % H_2O_2 for 1 h at 80 °C, to remove any organic impurities, then for 1 h at 80 °C in 1 M H_2SO_4 to ensure that the sulfonic groups of the polymer are protonated, and finally for 1 h in boiling Milli-Q water.

Commercial 40 wt % Pt/C (Sigma-Aldrich) was used as the cathode catalyst for all MEAs. Catalyst inks containing the dry powder, 30 wt % of the dry catalyst Nafion ionomer, and 1 mL of isopropanol were prepared.

Anode catalyst inks were prepared in a similar fashion. The Nafion ionomer was set at 20 wt % of the dry catalyst loading, and 2 mL of isopropanol was used. The catalyst loading on MEAs was set at 2 mg cm^{-2} for $Ir_xSn_{1-x}O_2$ and Sn/Ir catalysts. Variable loadings of commercial IrO_2 and iridium black loadings were used, as described in the Results and Discussion.

The catalyst inks were spray-coated on the membranes, which were fixed between two in-house designed aluminum plates that were heated at 60 °C. The geometric catalyst-coated area of membranes, corresponding to the cell area, was 4 cm^2. After spray coating the catalysts, the membranes were hot-pressed at 130 °C and 25 kg cm^{-2} for 3 min. Subsequently the catalyst-coated membranes were sandwiched between two gas diffusion layers (GDLs) consisting of 450 μm thick Pt-coated titanium felt plates. The assembly was then mounted in an in-house designed single PEM electrolysis cell with titanium collectors and single serpentine flow channels. For a higher corrosion resistance, the area of the collectors in contact with GDLs is gold-coated.

2.4. Electrochemical Experiments. Water electrolysis experiments were conducted at 80 °C. Milli-Q water was fed both to the anode and cathode compartments of the PEM cell at a flow rate of 1 mL min^{-1} using a peristaltic pump (Ismatec Reglo Digital). The water was preheated at 85 °C before passing through the PEM cell.

Linear sweep voltammetry experiments were conducted with a PGSTAT 302N potentiostat (Metrohm Autolab), equipped with a 20 A booster. The cell voltage was scanned in the 1.3−2.2 V range. The scan rate was set to 15 mV min^{-1}. During experiments, variations in the recorded current densities have been observed. These are typically caused by slight misalignments between the gas diffusion electrode and the catalyst-coated membrane or as a result of inhomogeneities during spray coating the catalysts over membranes. However, these variations did not exceed 10 mA/cm^2. Errors bars are therefore not indicated on the polarization curves. Electrochemical impedance spectroscopy experiments were conducted at 1.5 V, with a perturbation wave of 10 mV in the 16 kHz to 100 mHz frequency range. Spectra were fitted using the NOVA software. Galvanostatic chronoamperometry experiments were performed at 1 A cm^{-2} current density for 24 h.

3. RESULTS AND DISCUSSION

3.1. Iridium Oxide−Tin Oxide Catalysts Prepared by SCS. Several synthesis methods for IrO_2−SnO_2 OER catalysts based on the modified Adams fusion method, modified polyol method, and template-assisted synthesis are reported in the literature.[29,30,34,35] Often, the synthesis of nanosized iridium oxide powder catalysts involves a series of time- and resource-consuming steps. The SCS method can yield nanoparticulate oxide catalyst powders in one step, eliminating washing and separation procedures. This poses significant advantages in the context of reducing the CO_2 footprint of catalyst manufacturing and achieving a more sustainable chemical industry. We took this advantage of SCS and applied this method to prepare a series of IrO_2−SnO_2 catalysts with 10, 25, 50, 75, and 90 wt % SnO_2 content. The metal content was confirmed by X-ray photoelectron spectroscopy (XPS). We decided to vary SnO_2 in a broad range, to highlight the versatility of the SCS method and to investigate how the SnO_2 content in the powders influences the catalytic properties. The IrO_2−SnO_2 catalysts were tested for their oxygen evolution activity in a single PEM electrolysis cell, accompanying the hydrogen evolution reaction at the cathode.

3.1.1. Iridium Oxide−Tin Oxide Catalyst Characterization. The synthesized powders were characterized by X-ray diffraction (XRD), nitrogen physisorption, and TEM. The most significant observation in the XRD patterns of the catalysts is the shift of the most intense peaks compared to the

reference values for IrO_2 and SnO_2 (Figure 1). This shift is indicative of mixed oxide, more precisely solid solution,
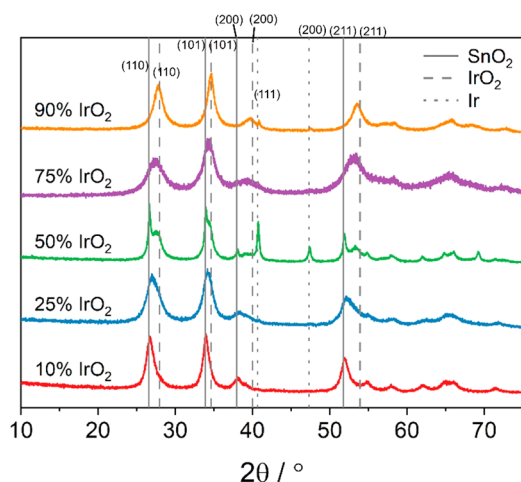

Figure 1. X-ray diffractograms of $Ir_xSn_{1-x}O_2$ powders synthesized by the SCS.

formation. IrO_2 and SnO_2 both crystallize in a tetragonal phase with $a = 0.4499$ nm and $c = 0.3146$ nm for IrO_2 and $a = 0.4738$ nm and $c = 0.31865$ nm for SnO_2, respectively.[36,37] Ionic radii of Ir^{4+} and Sn^{4+} are also similar, 0.077 and 0.083 nm, respectively. As pointed out by Xu et al., according to the Hume–Rothery theory, the formation of a solid solution of IrO_2 and SnO_2 should be possible.[29] The authors mention that metastable solid solutions of IrO_2 and SnO_2 are formed under well-defined composition and temperature conditions. More recently, Marshall et al. succeeded in obtaining a metastable solid solution of Ir–Sn oxides via a modified polyol method.[30] Interestingly, the authors found that the Adams fusion method yields a material with two distinct phases: an iridium-rich phase and a tin-rich phase. The reason for the formation of the solid solution is the formation of a highly mixed Ir–Sn phase during

synthesis, which is not achieved via the Adams fusion method. In a further study, Marshall et al. tested their Ir–Sn mixed oxide powders prepared by the polyol method in a PEM cell.[34] Unfortunately, the catalysts containing tin showed inferior performance compared to well-defined IrO_2 catalysts.

We performed lattice parameter refinement of X-ray diffractograms to determine the sample composition. A good agreement of the experimentally determined lattice parameter a with values predicted according to Vegard's law was found (Figure S1 of the Supporting Information). The formation of solid solutions, matching the Ir/Sn ratio calculated during synthesis, was confirmed. The surface area of the SCS-prepared samples, determined by nitrogen physisorption, varied between 18 and 43 m^2 g^{-1} (Table S1 and Figure S15 of the Supporting Information). No clear correlation was observed between the IrO_2 and SnO_2 ratios and the surface area of the catalyst powders.

Needle-like crystallites, similar to those previously observed in our work on solution combustion-prepared IrO_2–Al_2O_3 catalysts, were observed in TEM (Figure 2 and Figure S2 of the Supporting Information).[31] From EDS mapping, high dispersion and mostly uniform distribution of Ir and Sn throughout the particles can be observed (Figure 2 and Figure S3 of the Supporting Information). This is in good agreement with the findings from the XRD analysis, indicating the formation of an iridium–tin oxide solid solution.

3.1.2. $Ir_xSn_{1-x}O_2$: PEM Cell Performance and Overpotential Analysis. After the successful synthesis and the observation of mixed oxide formation, we proceeded with testing the samples in the PEM cell for their catalytic activity in the OER. For a fair comparison, we tested a series of MEAs containing commercial IrO_2 loadings comparable to $Ir_xSn_{1-x}O_2$ MEAs. The anode catalyst loading for $Ir_xSn_{1-x}O_2$ MEAs was fixed at 2 mg cm^{-2}. The loading of iridium oxide MEAs was set at 0.2, 0.5, 1, 1.5, and 2 mg cm^{-2}. The assessment of MEA performance was conducted by recording polarization curves in the 1.3–2.2 V cell voltage range (Figure 3 and Figure S4 of
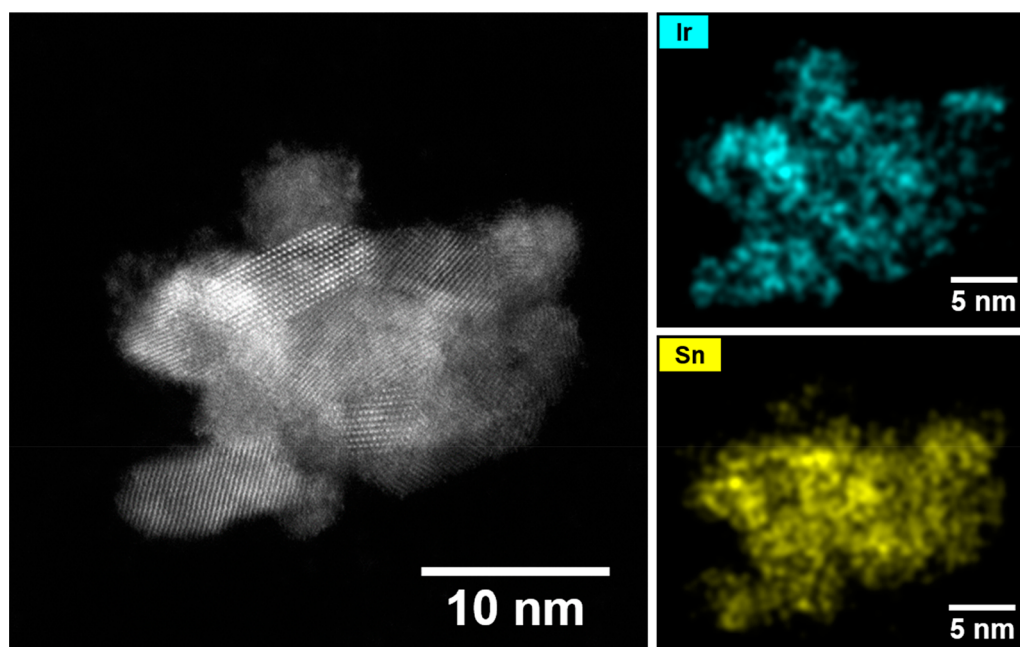

Figure 2. HRTEM micrograph of a $Ir_{0.75}Sn_{0.25}O_2$ catalyst synthesized by the SCS and EDS mapping of Sn and Ir.
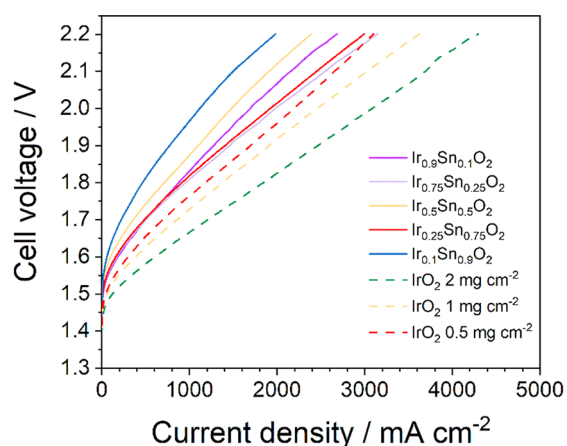
Figure 3. Polarization curves of $Ir_xSn_{1-x}O_2$ and commercial IrO_2 MEAs, with 0.75 mg cm^{-2} of a 40 wt % Pt/C cathode catalyst, Nafion 115, and 80 °C.

the Supporting Information). As a first observation, the inferior performance of $Ir_xSn_{1-x}O_2$ MEAs compared to commercial iridium oxide MEAs, even at low catalyst loadings, is noted. Interestingly, the $Ir_{0.25}Sn_{0.75}O_2$ and $Ir_{0.75}Sn_{0.25}O_2$ MEAs show a similar performance, despite the significant differences in Ir loading. The catalytic performance does not correlate with the surface area determined by N_2 physisorption (Table S1 and Figure S15 of the Supporting Information). The best performing catalyst $Ir_{0.75}Sn_{0.25}O_2$ exhibited the lowest Brunauer–Emmett–Teller (BET) surface area in the series.

To understand the origin of poorer performance and higher cell voltage when the SCS-synthesized materials were used, the

contribution of various overpotentials was decoupled by deconvoluting the polarization curves (Figure S5 of the Supporting Information).[38−40] The kinetic overpotential is accessible from the Tafel plot analysis of the iR-free polarization curves. The ohmic overpotential can be determined from the ohmic resistance measured by electrochemical impedance spectroscopy (EIS). It is characterized by a single parameter, the cell resistance determined from the high-frequency intercept (HFR) of impedance spectra measured for each MEA (Figure 4a and Figure S13 and Table S5 of the Supporting Information). Ohmic resistance values, together with the kinetic parameters for each MEA, are summarized in Table S3 of the Supporting Information. The thermodynamic cell voltage is determined using the Nernst equation. As the cell was operated at 80 °C, the calculated value of the thermodynamic potential is 1.18 V. The remaining overpotential contribution, after subtraction of the aforementioned terms, can be assumed to correspond to mass transport overpotential.[39]

The ohmic resistance of commercial iridium oxide MEAs increases linearly with a decreasing iridium oxide loading. This correlation has been observed and described in the literature. It can be explained by the decrease in catalyst layer thickness with loading, leading to a less contiguous and less uniform catalyst layer with a higher in-plane resistance.[41,42] For $Ir_xSn_{1-x}O_2$ MEAs, a similar trend was observed. In comparison to the commercial iridium oxide MEAs, recorded ohmic resistance values for $Ir_xSn_{1-x}O_2$ were higher for similar iridium oxide loadings. This is likely due to a lower electronic conductivity of $Ir_xSn_{1-x}O_2$ powders compared to IrO_2, as reported in the literature for IrO_2–TiO_2 powders and Ir–Sn mixed oxides.[34,43]
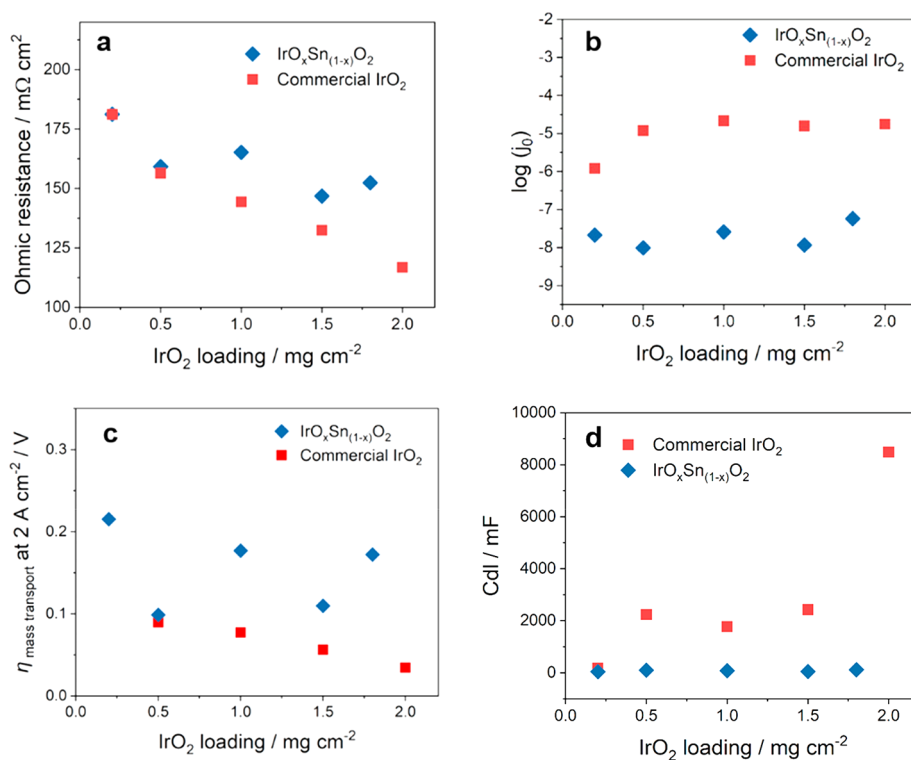

Figure 4. (a) Ohmic resistance determined by EIS, (b) logarithm of the exchange current density determined from iR-free Tafel plots, (c) mass transport overpotential at 2 A cm^{-2} current density, and (d) double-layer capacitance as a function of IrO_2 loading for $Ir_xSn_{1-x}O_2$ and commercial IrO_2 MEAs.

The kinetic overpotential is determined by two parameters: (i) the apparent Tafel slope, from which the reaction mechanism can be derived, and (ii) the exchange current density, which contains information about the intrinsic catalytic activity of the materials and available reaction sites. The apparent Tafel slopes for most of the tested MEAs exhibited values around $40-41$ mV dec^{-1}, in agreement with commonly reported literature values for iridium-based OER catalysts (Table S2).[44,45] $Ir_xSn_{1-x}O_2$ MEAs exhibited exchange current densities of 2 orders of magnitude lower than commercial IrO_2 MEAs (Figure 4b). The deconvolution of the activation overpotential shows that the mixed oxide powders have a significantly lower exchange current density activity for the OER compared to commercial IrO_2. On the basis of the remarkable differences observed between the commercial catalyst and the mixed oxide materials, this appears to be the critical parameter for the lower performance of $Ir_xSn_{1-x}O_2$ powders. This could be due to a difference in the electrochemically active surface area. For amorphous pure IrO_2 catalysts, it was reported that the presence of a hollandite structural motif translates into a higher catalytic activity compared to catalysts that exhibit solely a rutile structural motif.[46] In each series, a slight decrease in the exchange current density with decreasing iridium oxide loading is noted, suggesting a decrease in the number of available reaction sites.

For similar IrO_2 loadings, $Ir_xSn_{1-x}O_2$ MEAs exhibited approximately 100 mV higher mass transport overpotentials to reach 2 A cm^{-2} current density compared to that of commercial IrO_2 catalysts (Figure 4c). These differences could be caused by differences in porosity of the catalyst layer. Typically, ink formulations and ionomer content have an influence on catalyst layer porosity. As we focused solely on catalyst composition variation, other parameters were kept the same. It is possible that differences in crystallite morphology of $Ir_xSn_{1-x}O_2$ powders compared to commercial IrO_2 lead to changes in catalyst layer porosity. Optimization of parameters, such as the ionomer content, in catalyst inks or hot pressing could be able to improve mass transport overpotentials. This may cause evolved oxygen bubbles to become trapped or hinder their detachment from the catalyst surface and decrease water molecule transport to the catalyst surface.

On the basis of the deconvolution of the polarization curves, it is visible why the $Ir_{0.25}Sn_{0.75}O_2$ and $Ir_{0.75}Sn_{02.5}O_2$ samples show similar performance in the polarization curve. Despite the higher ohmic resistance, the $Ir_{0.25}Sn_{0.75}O_2$ MEA exhibits a lower mass transport overpotential, which could be caused by a favorable packing of powder in the catalyst layer.

Figure 4d shows the double-layer capacitance of the SCS materials and the commercial IrO_2 catalyst as a function of iridium loading on MEAs. The commercial iridium oxide catalyst exhibits a significantly higher double-layer capacitance, indicating an increased electrochemically active surface area compared to the $Ir_xSn_{1-x}O_2$ powders.

Stability experiments for $Ir_xSn_{1-x}O_2$ MEAs indicated that a performance loss becomes more significant with the SnO_2 content (Figure S6 of the Supporting Information). Geiger et al. reported SnO_2 leaching from doped tin oxide supports.[26] However, overnight acid treatment of catalysts by 1 M H_2SO_4 revealed no morphological and crystalline structure changes in TEM and XRD (Figure S17 of the Supporting Information). The stability experiment was performed at a 1 A cm^{-2} current density. In this region, the catalytic performance is determined by the slope of the linear part of the linear sweep

voltammogram (i.e., the ohmic resistance). Therefore, an increase in MEA resistance as a result of morphological changes of the ionomer structure and/or an increased porosity of the catalyst layer could cause the performance loss, although further detailed studies need to be performed to verify this hypothesis.

In summary, the performance of $Ir_xSn_{1-x}O_2$ MEAs is inferior to commercial IrO_2 MEAs as a result of a combination of effects: higher ohmic resistance, lower electrochemically active surface area, and hindered mass transport through the catalyst layer. The ohmic and mass transport overpotential at higher cell voltage could be reduced in principle by the addition of a conductive material or the optimization of catalyst layer deposition methods. Nevertheless, the electrochemically active surface area of $Ir_xSn_{1-x}O_2$ powders prepared by SCS is a factor that cannot be improved easily, making the mixed Ir—Sn oxides unsuitable for commercial application as OER catalysts.

3.2. Sn/Ir Catalysts Prepared by the Precipitation—Deposition Method. To investigate the promotional effect of Sn in Ir-based OER catalysts further, we explored different types of catalyst powders. The focus was switched from iridium oxide to metallic iridium, which is not as active as iridium oxide but provides satisfactory performance in the OER. In our approach, we steered away from commonly reported methods, in which the active iridium/iridium oxide component is deposited over the support material (SnO_2, antimony tin oxide, indium tin oxide, etc.).[13,28,47,48] Instead, we started with iridium black (i.e., metallic Ir) powder, over which we deposited tin, via the precipitation—deposition method. In the anodic conditions of the PEM electrolyzer, deposited Sn would eventually oxidize to SnO_2. With this nanostructured Ir—Sn composite, the promotional effect of SnO_2 on iridium-based OER catalysts, which was reported in the literature but was not observed for $Ir_xSn_{1-x}O_2$ MEAs, will be investigated further. The approach could lead to an enhancement of the Ir—Sn contact without the formation of a mixed oxide of solid solutions, because the synthesis method that we adopted cannot yield the formation of these by design.

With these in mind, we synthesized a series of catalysts with 5, 7, 10, 15, 20, 30, 50, and 90 wt % Sn coated over Ir black (denoted as Sn/Ir). We took an approach similar to that for IrO_2—SnO_2 powders and decided to investigate a broad range of iridium loadings. We were especially interested in the promotional effect of Sn. For this reason, a stronger emphasis was put on powders with low Sn loadings (10—20 wt %), where the highest differences were expected. A series of materials with smaller differences in Sn loading in this range were prepared and investigated. We prepared and tested the Sn/Ir MEAs with 2 mg cm^{-2} catalyst loading, containing iridium loadings of 1.9, 1.86, 1.8, 1.7, 1.6, 1.4, 1, and 0.2 mg cm^{-2}, respectively. For the sake of comparison and to observe the effect of Sn addition, we also tested a series of MEAs containing solely iridium black powder with loadings of 0.2, 0.5, 0.7, 1, 1.5, and 2 mg cm^{-2}.

3.2.1. Sn/Ir Catalysts: Catalyst Characterization. XRD patterns of Sn/Ir catalysts exhibit reflections specific to metallic iridium (Figure 5). Ir crystallite size determined using the Scherrer equation is ca. 3 nm. No peaks characteristic of Sn or SnO_2 could be observed for the powders with Sn loading up to 20%. This indicates that Sn/SnO_2 is present in an amorphous phase or in a very small crystallite size and, thus, is not detectable by XRD. Only for the catalyst with the highest Sn loading, 90 wt %, broad peaks characteristic for Sn were
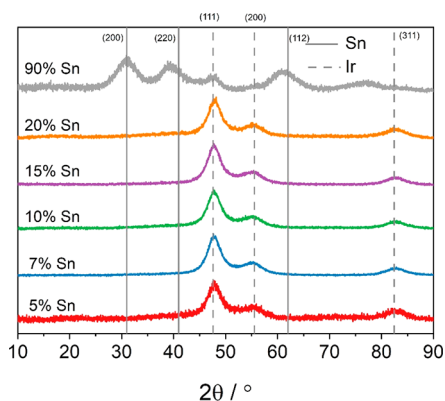
Figure 5. XRD patterns of Sn/Ir powders.

detected. This suggests that only at very high loadings does Sn/SnO$_2$ crystallize with a long-range order, although the crystallite size is very small (ca. 2 nm).

Agglomerates consisting of <5 nm crystallites and an amorphous phase were observed in TEM (Figures S7 and S8 of the Supporting Information). Energy-dispersive X-ray spectra in Figures S7 and S8 of the Supporting Information reveal the presence of both iridium and tin in the sample. Both iridium and tin were detected by elemental mapping, and Figure S7 of the Supporting Information shows a high dispersion of the two elements in the amorphous phase. A good contact between the two phases was therefore achieved.

To clarify the composition of the crystallites present in the sample, we measured *d* spacing of crystalline regions from HRTEM, revealing the presence of iridium, tin, iridium oxide, and tin oxide (Figure 6 and Figures S9−S11 of the Supporting Information). Lattice *d* spacings were abstracted from the fast Fourier transformation (FFT) of lattice fringes in areas shown in red in Figure 6. Areas 1 and 2 in Figure 6 could correspond to the IrO$_2$ (110) plane, with a lattice spacing of 0.32 nm. In areas 3 and 4 in Figure 6, the determined lattice spacing of 0.34 nm could indicate the SnO$_2$ (110) plane. The (200) plane of SnO$_2$, with a lattice spacing of 0.24 nm, and the (211) plane of Sn, with a lattice spacing of 0.20 nm, were also identified (Figures S9 and S10 of the Supporting Information). The preparation of the catalysts did not involve any oxidation steps,

and metallic iridium is not expected to oxidize under ambient conditions. However, given the high surface area of the materials and the fact that the samples were not stored under an inert atmosphere, the formation of an ill-structured sub-oxide is possible (Table S4 of the Supporting Information). Furthermore, TEM experiments were conducted at a later time compared to XRD, which might explain why IrO$_2$ crystallites were not identified in XRD patterns. Sn forms a protective oxide layer on the surface, preventing its oxidation.

3.2.2. Sn/Ir Catalysts: PEM Cell Performance and Overpotential Analysis. Polarization curves in PEM water electrolysis using Sn/Ir catalysts at the anode were recorded in the 1.3−2.2 V cell voltage range (Figure 7). The most
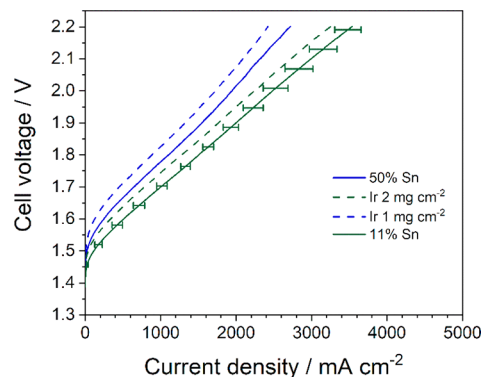

Figure 7. Polarization curves of Sn/Ir MEAs and Ir black MEAs, with 0.75 mg cm^{-2} of a 40 wt % Pt/C cathode catalyst, Nafion 115, and 80 °C. The error bars in the polarization curve represent variations in the current density of MEAs as a function of Sn loading in MEAs with 10−20 wt % Sn.

notable observation in the polarization curves is that Sn addition leads to higher current density at the same cell voltage compared to Ir black MEAs with similar Ir loadings.

To gain further insights into the underlying causes of the performance enhancement as a result of Sn addition, we performed overpotential analysis (Figure 8).

The ohmic resistance of iridium black MEAs is found to be almost independent of the Ir loading (Figure 8a and Figure S14 and Table S5 of the Supporting Information). Sn/Ir MEAs
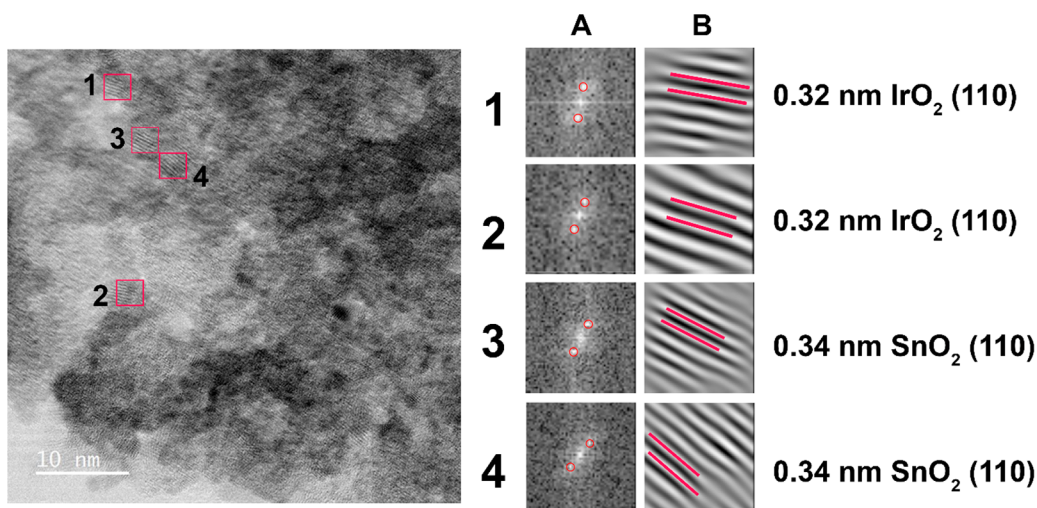

Figure 6. HRTEM micrograph of a 10 wt % Sn/Ir catalyst, calculated *d* spacing, and corresponding planes for selected areas.
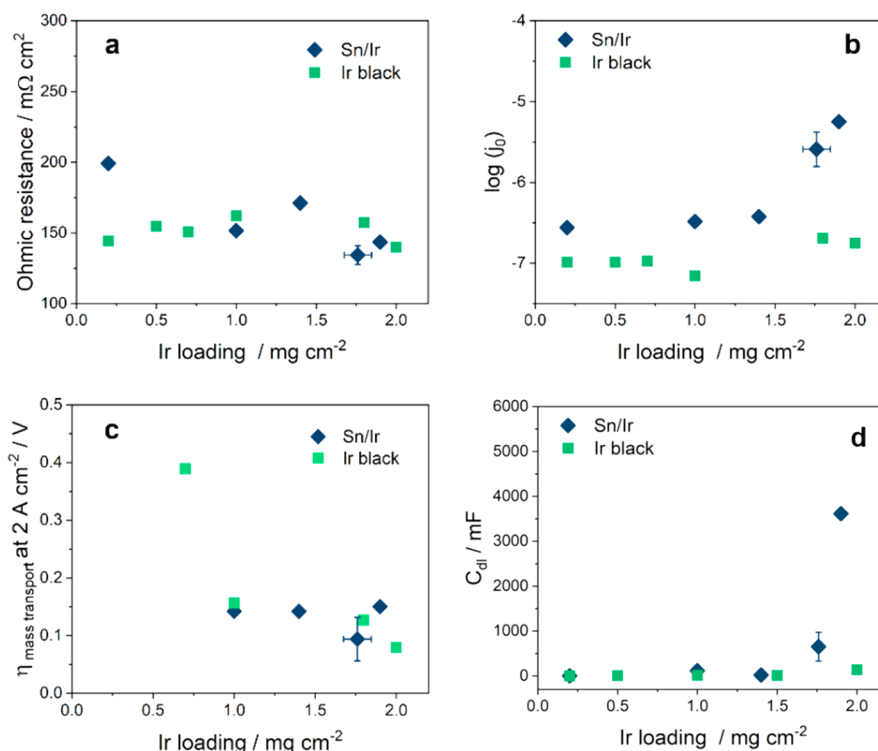
Figure 8. (a) Ohmic resistance determined by EIS, (b) logarithm of the exchange current density determined from *iR*-free Tafel plots, (c) mass transport overpotential at 2 A cm^{-2} current density, and (d) double-layer capacitance as a function of iridium loading for Sn/Ir and Ir black MEAs. The error bars in the figures represent variations in current density of MEA as a function of Sn loading in MEAs with <20 wt % Sn.

exhibit slightly lower ohmic resistance at higher Ir loading. Nevertheless, the difference in the ohmic resistance values between the Sn/Ir MEAs and Ir black MEAs is small.

Looking at the kinetic overpotential, both the apparent Tafel slopes of the Sn/Ir MEAs and iridium black MEAs display similar values of 39−40 mV dec^{-1} (Table S3 of the Supporting Information), in agreement with the literature values, suggesting that oxygen evolution follows the same reaction mechanism for both types of catalysts. The MEAs with the highest tin loading (90 wt %) and equivalent Ir loading of iridium black (0.2 mg cm^{-2}) show significantly higher Tafel slope and represent an exception (Table S3 of the Supporting Information). The higher apparent Tafel slope observed does not necessarily point to a different reaction mechanism, but as reported by Bernt et al., it could suggest additional voltage losses for the very thin and inhomogeneous catalyst layer, which we also visually observed during MEA preparation.[42] Additionally, it is possible that the Pt-coated titanium gas diffusion layers (GDLs) were partially in contact with the Nafion membrane directly, particularly for the 90 wt % Sn MEA as a result of the thin catalyst layer, and might have exhibited some OER catalytic activity themselves, altering the value of the apparent Tafel slope.

The exchange current density displayed by Sn/Ir MEAs with <30 wt % Sn catalysts is 1 order of magnitude higher compared to iridium black MEAs (Figure 8b), illustrating the strong promotional effect of Sn in the OER. The exchange current density decreases slightly with iridium loading on both types of MEAs, which can be attributed to the decrease in the active catalyst surface area, leading to a lower number of surface reaction sites.

Figure 8c shows no effect of Sn addition on mass transport overpotentials, with similar values for all MEAs.

In Figure 8d, the electrochemically active surface area as a function of Ir loading on MEAs is presented. Sn addition up to 10 wt % to the powders increases the electrochemically active surface area by 1 order of magnitude (Figure S14 and Table S5 of the Supporting Information). This suggests that Sn acts as a spacer between catalyst particles, increasing the number of available iridium reaction sites, which leads to superior performance compared to Ir black MEAs.

Furthermore, the stability of the nanostructured Sn/Ir catalyst was investigated. Chronopotentiometry experiments at 1 A cm^{-2} for 24 h were conducted to investigate how the stability of the 10 wt % Sn/Ir catalyst compares to Ir black (Figure S12 of the Supporting Information). No increase in cell voltage could be observed during experiments, showing that Sn addition does not affect the long-term stability of MEAs. Scanning electron micrographs of the MEAs after the long-term stability test were recorded (Figure S16 of the Supporting Information). A uniform distribution of Sn was observed for MEAs with <20% Sn loading. The 90% Sn/Ir MEA exhibited aggregates of Sn, indicating tin migration at high loadings.

To summarize, we were able to prepare iridium tin OER catalysts, which valorize the promotional effect induced by the tin addition. The primary parameters at which the Sn/Ir MEAs excel are the lower kinetic overpotential and improved mass transport and, to a lesser extent, the lower ohmic resistance compared to iridium black MEAs. A tin loading of around 11 wt % appears to be the optimum for achieving the superior performance with excellent long-term stability. MEAs with tin loadings higher than 20 wt % exhibited exchange current densities of 1 order of magnitude lower. It is possible that at high tin loadings the surface of iridium particles becomes

covered with tin oxide to a level at which the promotional effect is counterbalanced by a lower availability of surface sites.

4. CONCLUSION

We investigated the performance of two types of iridium-based OER catalysts in a PEM electrolysis cell: $Ir_xSn_{1-x}O_2$ catalysts were prepared by the SCS method, and Sn/Ir catalysts were prepared by the precipitation−deposition method. The goal of the study was to investigate whether addition of tin to iridium-based catalysts improves the cell performance and to elucidate the structural factors to induce Sn−Ir synergistic effects. The MEAs prepared by the SCS method did not show a superior performance compared to MEAs with commercial iridium oxide as a result of a higher ohmic resistance of the catalysts as well as a lower electrochemically active surface area of the materials. In contrast, Sn/Ir MEAs performed better than the counterpart, i.e., iridium black MEAs. The main contribution for the better performance is the higher exchange current density for Sn/Ir MEAs, which is caused by a higher number of available surface reaction sites, leading to a higher degree of iridium utilization. Sn addition did not affect the mass transport overpotentials of the MEAs. Further *operando* investigations of these catalysts are required to confirm or disprove this hypothesis, which we will cover in our future works on the subject. Our results illustrate that the catalyst synthesis method, spatial distribution and mixing of Sn and Ir, and oxidation state of iridium are crucial to induce Sn−Ir synergy.

■ ASSOCIATED CONTENT

ⓈⅠ Supporting Information

The Supporting Information is available free of charge at https://pubs.acs.org/doi/10.1021/acs.energyfuels.3c03238.

> Lattice parameter as a function of the solid solution composition for SCS catalysts, XRD and TEM characterization, EDS spectra, polarization curves of IrO_2 prepared by SCS and commercial IrO_2 powder, overpotential contributions, BET surface area, kinetic parameters from Tafel plot analysis, and chronopotentiometry experiments (PDF)

■ AUTHOR INFORMATION

Corresponding Author

Atsushi Urakawa − *Catalysis Engineering, Department of Chemical Engineering, Delft University of Technology, 2629 HZ Delft, Netherlands;* ⓞ orcid.org/0000-0001-7778-4008; Email: a.urakawa@tudelft.nl

Authors

Sorin Bunea − *Catalysis Engineering, Department of Chemical Engineering, Delft University of Technology, 2629 HZ Delft, Netherlands*

Min Li − *Catalysis Engineering, Department of Chemical Engineering, Delft University of Technology, 2629 HZ Delft, Netherlands*

Ezgi Demiröz − *Catalysis Engineering, Department of Chemical Engineering, Delft University of Technology, 2629 HZ Delft, Netherlands;* ⓞ orcid.org/0000-0001-6788-2990

Peng Zeng − *Scientific Center for Optical and Electron Microscopy (ScopeM), ETH Zurich, 8093 Zurich, Switzerland*

Marc Georg Willinger − *Scientific Center for Optical and Electron Microscopy (ScopeM), ETH Zurich, 8093 Zurich, Switzerland;* ⓞ orcid.org/0000-0002-9996-7953

Complete contact information is available at:
https://pubs.acs.org/10.1021/acs.energyfuels.3c03238

Notes

The authors declare no competing financial interest.

■ ACKNOWLEDGMENTS

■ REFERENCES

(1) International Energy Agency (IEA). *Global Energy Review 2020*; IEA: Paris, France, 2020.

(2) Bockris, J. O. M. The origin of ideas on a Hydrogen Economy and its solution to the decay of the environment. *Int. J. Hydrogen Energy* **2002**, *27* (7), 731−740.

(3) Carmo, M.; Fritz, D. L.; Mergel, J.; Stolten, D. A comprehensive review on PEM water electrolysis. *Int. J. Hydrogen Energy* **2013**, *38* (12), 4901−4934.

(4) Saba, S. M.; Müller, M.; Robinius, M.; Stolten, D. The investment costs of electrolysis—A comparison of cost studies from the past 30 years. *Int. J. Hydrogen Energy* **2018**, *43* (3), 1209−1223.

(5) Ao, K.; Wei, Q.; Daoud, W. A. MOF-Derived Sulfide-Based Electrocatalyst and Scaffold for Boosted Hydrogen Production. *ACS Appl. Mater. Interfaces* **2020**, *12* (30), 33595−33602.

(6) Bhanja, P.; Kim, Y.; Paul, B.; Kaneti, Y. V.; Alothman, A. A.; Bhaumik, A.; Yamauchi, Y. Microporous nickel phosphonate derived heteroatom doped nickel oxide and nickel phosphide: Efficient electrocatalysts for oxygen evolution reaction. *Chem. Eng. J.* **2021**, *405*, 126803.

(7) Guo, Y.; Zhang, C.; Zhang, J.; Dastafkan, K.; Wang, K.; Zhao, C.; Shi, Z. Metal-Organic Framework-Derived Bimetallic NiFe Selenide Electrocatalysts with Multiple Phases for Efficient Oxygen Evolution Reaction. *ACS Sustainable Chem. Eng.* **2021**, *9* (5), 2047−2056.

(8) Septiani, N. L. W.; Kaneti, Y. V.; Fathoni, K. B.; Guo, Y.; Ide, Y.; Yuliarto, B.; Jiang, X.; Nugraha; Dipojono, H. K.; Golberg, D.; Yamauchi, Y. Tailorable nanoarchitecturing of bimetallic nickel-cobalt hydrogen phosphate via the self-weaving of nanotubes for efficient oxygen evolution. *J. Mater. Chem. A* **2020**, *8* (6), 3035−3047.

(9) Hu, S.; Wang, S.; Feng, C.; Wu, H.; Zhang, J.; Mei, H. Novel MOF-Derived Nickel Nitride as High-Performance Bifunctional Electrocatalysts for Hydrogen Evolution and Urea Oxidation. *ACS Sustainable Chem. Eng.* **2020**, *8* (19), 7414−7422.

(10) Septiani, N. L. W.; Kaneti, Y. V.; Guo, Y.; Yuliarto, B.; Jiang, X.; Ide, Y.; Nugraha, N.; Dipojono, H. K.; Yu, A.; Sugahara, Y.; Golberg, D.; Yamauchi, Y. Holey Assembly of Two-Dimensional Iron-Doped Nickel-Cobalt Layered Double Hydroxide Nanosheets for Energy Conversion Application. *ChemSusChem* **2020**, *13* (6), 1645−1655.

(11) Oakton, E.; Lebedev, D.; Povia, M.; Abbott, D. F.; Fabbri, E.; Fedorov, A.; Nachtegaal, M.; Copéret, C.; Schmidt, T. J. IrO_2-TiO_2: A High-Surface-Area, Active, and Stable Electrocatalyst for the Oxygen Evolution Reaction. *ACS Catal.* **2017**, *7* (4), 2346−2352.

(12) Böhm, D.; Beetz, M.; Schuster, M.; Peters, K.; Hufnagel, A. G.; Döblinger, M.; Böller, B.; Bein, T.; Fattakhova-Rohlfing, D. Efficient OER Catalyst with Low Ir Volume Density Obtained by Homogeneous Deposition of Iridium Oxide Nanoparticles on Macroporous Antimony-Doped Tin Oxide Support. *Adv. Funct. Mater.* **2020**, *30* (1), 1906670.

(13) Hartig-Weiss, A.; Miller, M.; Beyer, H.; Schmitt, A.; Siebel, A.; Freiberg, A. T. S.; Gasteiger, H. A.; El-Sayed, H. A. Iridium Oxide Catalyst Supported on Antimony-Doped Tin Oxide for High Oxygen Evolution Reaction Activity in Acidic Media. *ACS Appl. Nano Mater.* **2020**, *3* (3), 2185−2196.

(14) Park, J. E.; Kim, S.; Kim, O.-H.; Ahn, C.-Y.; Kim, M.-J.; Kang, S. Y.; Jeon, T. I.; Shim, J.-G.; Lee, D. W.; Lee, J. H.; Cho, Y.-H.; Sung, Y.-E. Ultra-low loading of IrO₂ with an inverse-opal structure in a polymer-exchange membrane water electrolysis. *Nano Energy* **2019**, *58*, 158−166.

(15) Hegge, F.; Lombeck, F.; Cruz Ortiz, E.; Bohn, L.; von Holst, M.; Kroschel, M.; Hübner, J.; Breitwieser, M.; Strasser, P.; Vierrath, S. Efficient and Stable Low Iridium Loaded Anodes for PEM Water Electrolysis Made Possible by Nanofiber Interlayers. *ACS Appl. Energy Mater.* **2020**, *3* (9), 8276−8284.

(16) Rozain, C.; Mayousse, E.; Guillet, N.; Millet, P. Influence of iridium oxide loadings on the performance of PEM water electrolysis cells: Part II—Advanced oxygen electrodes. *Appl. Catal., B* **2016**, *182*, 123−131.

(17) Polonský, J.; Kodým, R.; Vágner, P.; Paidar, M.; Bensmann, B.; Bouzek, K. Anodic microporous layer for polymer electrolyte membrane water electrolysers. *J. Appl. Electrochem.* **2017**, *47* (10), 1137−1146.

(18) Pham, C. V.; Bühler, M.; Knöppel, J.; Bierling, M.; Seeberger, D.; Escalera-López, D.; Mayrhofer, K. J. J.; Cherevko, S.; Thiele, S. IrO₂ coated TiO₂ core-shell microparticles advance performance of low loading proton exchange membrane water electrolyzers. *Appl. Catal., B* **2020**, *269*, 118762.

(19) Nong, H. N.; Gan, L.; Willinger, E.; Teschner, D.; Strasser, P. IrOₓ core-shell nanocatalysts for cost- and energy-efficient electrochemical water splitting. *Chem. Sci.* **2014**, *5* (8), 2955−2963.

(20) Siracusano, S.; Baglio, V.; Stassi, A.; Ornelas, R.; Antonucci, V.; Aricò, A. S. Investigation of IrO₂ electrocatalysts prepared by a sulfite-couplex route for the O₂ evolution reaction in solid polymer electrolyte water electrolyzers. *Int. J. Hydrogen Energy* **2011**, *36* (13), 7822−7831.

(21) Lim, J.; Park, D.; Jeon, S. S.; Roh, C.-W.; Choi, J.; Yoon, D.; Park, M.; Jung, H.; Lee, H. Ultrathin IrO₂ Nanoneedles for Electrochemical Water Oxidation. *Adv. Funct. Mater.* **2018**, *28* (4), 1704796.

(22) Sharma, R.; Gyergyek, S.; Andersen, S. M. Environmentally and Industrially Friendly Recycling of Platinum Nanoparticles Through Electrochemical Dissolution-Electrodeposition in Acid-Free/Dilute Acidic Electrolytes. *ChemSusChem* **2018**, *11* (21), 3742−3750.

(23) Carmo, M.; Keeley, G. P.; Holtz, D.; Grube, T.; Robinius, M.; Müller, M.; Stolten, D. PEM water electrolysis: Innovative approaches towards catalyst separation, recovery and recycling. *Int. J. Hydrogen Energy* **2019**, *44* (7), 3450−3455.

(24) Liu, G.; Xu, J.; Wang, Y.; Wang, X. An oxygen evolution catalyst on an antimony doped tin oxide nanowire structured support for proton exchange membrane liquid water electrolysis. *J. Mater. Chem. A* **2015**, *3* (41), 20791−20800.

(25) Oh, H.-S.; Nong, H. N.; Reier, T.; Gliech, M.; Strasser, P. Oxide-supported Ir nanodendrites with high activity and durability for the oxygen evolution reaction in acid PEM water electrolyzers. *Chem. Sci.* **2015**, *6* (6), 3321−3328.

(26) Geiger, S.; Kasian, O.; Mingers, A. M.; Mayrhofer, K. J. J.; Cherevko, S. Stability limits of tin-based electrocatalyst supports. *Sci. Rep.* **2017**, *7* (1), 4595.

(27) Oh, H.-S.; Nong, H. N.; Reier, T.; Bergmann, A.; Gliech, M.; Ferreira de Araújo, J.; Willinger, E.; Schlögl, R.; Teschner, D.; Strasser, P. Electrochemical Catalyst-Support Effects and Their Stabilizing Role for IrOₓ Nanoparticle Catalysts during the Oxygen Evolution Reaction. *J. Am. Chem. Soc.* **2016**, *138* (38), 12552−12563.

(28) Saveleva, V. A.; Wang, L.; Kasian, O.; Batuk, M.; Hadermann, J.; Gallet, J. J.; Bournel, F.; Alonso-Vante, N.; Ozouf, G.; Beauger, C.; Mayrhofer, K. J. J.; Cherevko, S.; Gago, A. S.; Friedrich, K. A.; Zafeiratos, S.; Savinova, E. R. Insight into the Mechanisms of High Activity and Stability of Iridium Supported on Antimony-Doped Tin Oxide Aerogel for Anodes of Proton Exchange Membrane Water Electrolyzers. *ACS Catal.* **2020**, *10* (4), 2508−2516.

(29) Xu, J.; Liu, G.; Li, J.; Wang, X. The electrocatalytic properties of an IrO₂/SnO₂ catalyst using SnO₂ as a support and an assisting reagent for the oxygen evolution reaction. *Electrochim. Acta* **2012**, *59*, 105−112.

(30) Marshall, A.; Børresen, B.; Hagen, G.; Tsypkin, M.; Tunold, R. Preparation and characterisation of nanocrystalline IrₓSn₁₋ₓO₂ electrocatalytic powders. *Mater. Chem. Phys.* **2005**, *94* (2), 226−232.

(31) Chourashiya, M. G.; Urakawa, A. Solution combustion synthesis of highly dispersible and dispersed iridium oxide as an anode catalyst in PEM water electrolysis. *J. Mater. Chem. A* **2017**, *5* (10), 4774−4778.

(32) Varma, A.; Mukasyan, A. S.; Rogachev, A. S.; Manukyan, K. V. Solution Combustion Synthesis of Nanoscale Materials. *Chem. Rev.* **2016**, *116* (23), 14493−14586.

(33) Grigoriev, S. A.; Millet, P.; Dzhus, K. A.; Middleton, H.; Saetre, T. O.; Fateev, V. N. Design and characterization of bi-functional electrocatalytic layers for application in PEM unitized regenerative fuel cells. *Int. J. Hydrogen Energy* **2010**, *35* (10), 5070−5076.

(34) Marshall, A.; Børresen, B.; Hagen, G.; Tsypkin, M.; Tunold, R. Electrochemical characterisation of IrₓSn₁₋ₓO₂ powders as oxygen evolution electrocatalysts. *Electrochim. Acta* **2006**, *51* (15), 3161−3167.

(35) Li, G.; Yu, H.; Yang, D.; Chi, J.; Wang, X.; Sun, S.; Shao, Z.; Yi, B. Iridium-Tin oxide solid-solution nanocatalysts with enhanced activity and stability for oxygen evolution. *J. Power Sources* **2016**, *325*, 15−24.

(36) Goldschmidt, V. M. Die Gesetze der Krystallochemie. *Naturwissenschaften* **1926**, *14* (21), 477−485.

(37) Baur, W. H.; Khan, A. A. Rutile-type compounds. IV. SiO₂, GeO₂ and a comparison with other rutile-type structures. *Acta Crystallogr., Sect. B: Struct. Crystallogr. Cryst. Chem.* **1971**, *27* (11), 2133−2139.

(38) Falcão, D. S.; Pinto, A. M. F. R. A review on PEM electrolyzer modelling: Guidelines for beginners. *J. Cleaner Prod.* **2020**, *261*, 121184.

(39) Schuler, T.; Schmidt, T. J.; Büchi, F. N. Polymer Electrolyte Water Electrolysis: Correlating Performance and Porous Transport Layer Structure: Part II. Electrochemical Performance Analysis. *J. Electrochem. Soc.* **2019**, *166* (10), F555−F565.

(40) Ojong, E. T.; Kwan, J. T. H.; Nouri-Khorasani, A.; Bonakdarpour, A.; Wilkinson, D. P.; Smolinka, T. Development of an experimentally validated semi-empirical fully-coupled performance model of a PEM electrolysis cell with a 3-D structured porous transport layer. *Int. J. Hydrogen Energy* **2017**, *42* (41), 25831−25847.

(41) Rozain, C.; Mayousse, E.; Guillet, N.; Millet, P. Influence of iridium oxide loadings on the performance of PEM water electrolysis cells: Part I-Pure IrO₂-based anodes. *Appl. Catal., B* **2016**, *182*, 153−160.

(42) Bernt, M.; Siebel, A.; Gasteiger, H. A. Analysis of Voltage Losses in PEM Water Electrolyzers with Low Platinum Group Metal Loadings. *J. Electrochem. Soc.* **2018**, *165* (5), F305−F314.

(43) Oakton, E.; Lebedev, D.; Fedorov, A.; Krumeich, F.; Tillier, J.; Sereda, O.; Schmidt, T. J.; Copéret, C. A simple one-pot Adams method route to conductive high surface area IrO₂-TiO₂ materials. *New J. Chem.* **2016**, *40* (2), 1834−1838.

(44) Zhao, Y.; Vargas-Barbosa, N. M.; Hernandez-Pagan, E. A.; Mallouk, T. E. Anodic Deposition of Colloidal Iridium Oxide Thin Films from Hexahydroxyiridate(IV) Solutions. *Small* **2011**, *7* (14), 2087−2093.

(45) Shinagawa, T.; Garcia-Esparza, A. T.; Takanabe, K. Insight on Tafel slopes from a microkinetic analysis of aqueous electrocatalysis for energy conversion. *Sci. Rep.* **2015**, *5* (1), 13801.

(46) Willinger, E.; Massué, C.; Schlögl, R.; Willinger, M. G. Identifying Key Structural Features of IrOₓ Water Splitting Catalysts. *J. Am. Chem. Soc.* **2017**, *139* (34), 12093−12101.

(47) Lebedev, D.; Ezhov, R.; Heras-Domingo, J.; Comas-Vives, A.; Kaeffer, N.; Willinger, M.; Solans-Monfort, X.; Huang, X.; Pushkar, Y.; Copéret, C. Atomically Dispersed Iridium on Indium Tin Oxide Efficiently Catalyzes Water Oxidation. *ACS Cent. Sci.* **2020**, *6* (7), 1189−1198.

(48) Da Silva, G. C.; Venturini, S. I.; Zhang, S.; Löffler, M.; Scheu, C.; Mayrhofer, K. J. J.; Ticianelli, E. A.; Cherevko, S. Oxygen Evolution Reaction on Tin Oxides Supported Iridium Catalysts: Do We Need Dopants? *ChemElectroChem* **2020**, *7* (10), 2330−2339.